SCIENCE CHINA
Information Sciences

• RESEARCH PAPER •

June 2019, Vol. 62 062406:1–062406:8
https://doi.org/10.1007/s11432-017-9472-x

Systematic calibration of drift diffusion model for InGaAs MOSFETs in quasi-ballistic regime

Shaoyan DI[1], Lei SHEN[1], Pengying CHANG[1], Kai ZHAO[3,1*], Tiao LU[2], Gang DU[1] & Xiaoyan LIU[1*]

[1]*Institute of Microelectronics, Peking University, Beijing* 100871*, China;*
[2]*CAPT, HEDPS, IFSA Collaborative Innovation Center of MoE, LMAM and School of Mathematical Sciences, Peking University, Beijing* 100010*, China;*
[3]*School of Information and Communication, Beijing Information Science and Technology University, Beijing* 100871*, China*

Received 12 February 2018/Revised 7 May 2018/Accepted 29 May 2018/Published online 1 March 2019

Abstract This paper proposes a systematic procedure to calibrate the parameters of the drift-diffusion (DD) model for a performance evaluation of InGaAs MOSFETs in the quasi-ballistic regime. The simulation results of a deterministic multi-subband Boltzmann transport equation (BTE) solver serve as the standard. The DD model is calibrated both under low and high electric fields. The electrostatic characteristics, low field mobility model, and high field saturation model are calibrated in proper sequence, and a good agreement among the drive current, carrier distribution, and velocity distribution are achieved between the results of the calibrated DD model and the BTE solver. The proposed calibration procedure can also be employed in devices made of other materials.

Keywords drift-diffusion model, calibration, Boltzmann transport equation, BTE, ballistic transport, high field, InGaAs MOSFET

Citation Di S Y, Shen L, Chang P Y, et al. Systematic calibration of drift diffusion model for InGaAs MOSFETs in quasi-ballistic regime. Sci China Inf Sci, 2019, 62(6): 062406, https://doi.org/10.1007/s11432-017-9472-x

1 Introduction

With the continuous development of semiconductor technologies, it is indispensable to make a performance prediction of a device using technology computer aided design (TCAD) tools prior to fabrication. However, some effects appearing in modern devices, such as a velocity overshoot and non-local transport, which are brought about by continuously scaling down, cannot be considered by the conventional drift-diffusion (DD) model employed through TCAD tools. Moreover, carrier transport in modern nano-scale devices shows a ballistic feature [1, 2]. The drive current of the MOSFET is not only restricted by the pinch-off near the drain, but also more crucially by the injection velocity at the virtual source [3, 4]. This phenomenon further deteriorates the accuracy of the DD model in predicting the performance of nano-scale MOSFETs.

As a more accurate tool, the deterministic Boltzmann transport equation (BTE) solver describes the velocity overshoot and ballistic transport physically because it captures every microscopic detail of the scattering mechanisms during the transport process. However, it is considerably time consuming to solve the BTE, despite the dimensions of the modern device being only within a range of deca-nanometers.

* Corresponding author (email: zhaokaipku@gmail.com, xyliu@ime.pku.edu.cn)

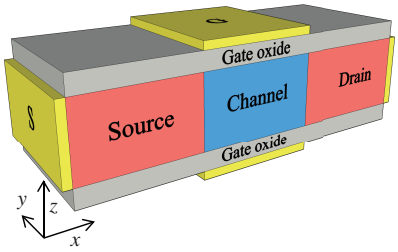

Figure 1 (Color online) Schematic of the simulated device structure.

Table 1 Structural parameters of the sample

Parameter	Value
Channel length	20 nm
S/D length	10 nm
Effective oxide thickness (EOT)	1 nm
Film thickness	5 nm
Channel doping	10^{17} cm^{-3}
S/D doping	5×10^{19} cm^{-3}

To improve the accuracy of TCAD tools without lifting the time consumption, it is necessary to calibrate the DD model employed by the commercial TCAD tools using the BTE simulator. Many studies have been conducted on DD model calibration for Si devices [5–7] because Si is still the main stream material used in MOSFETs. Recently, III-V materials, particularly for InGaAs MOSFETs, have gained further attention [8,9] because they show high mobility and a gradually improved surface quality [10]. Such materials are considered the most promising competitors for high-speed and low-power next generation devices, and some of them have been employed in high-speed and high-frequency systems [11]. A number of low field mobility models of InGaAs MOSFETs have been proposed [12]. However, the DD model under a high longitudinal electronic field in commercial TCAD tools for III-V materials has not been carefully calibrated. Moreover, the ballistic feature of ultra-short III-V MOSFETs is more obvious than that in Si devices, which means these conventional models cannot be used directly to predict the performance of III-V devices. In this study, we calibrate a DD model for short channel InGaAs MOSFETs operating in the quasi-ballistic regime under both low and high fields, and propose a standard procedure.

2 Simulation method

The results of a deterministic multi-subband Boltzmann transport equation (MSBTE) device simulator [13–15] have been used as the standard. A parabolic band structure is employed, and for InGaAs, we have considered the Γ valley and 4-fold degenerate L valleys. The quantum confinement effect is taken into account by solving a self-consistent Schrödinger-Poisson equation. We have considered acoustic phonon scattering (AP), intra-valley optical phonon scattering (OP) [16], inter-valley optical scattering (Γ-L and L-L), polar optical phonon scattering (POP), and surface roughness scattering (SR) [17]. The parameters of the band structure and scattering mechanisms are according to [18]. Moreover, the Pauli exclusion principle is also considered.

A double-gate InGaAs MOSFET with a channel length of 20 nm is chosen as the sample to demonstrate the calibration procedure. A schematic of the device structure is shown in Figure 1, and other structural parameters of the sample are listed in Table 1.

3 DD model calibration

Figure 2 shows a flow chart of the calibration procedure. We divided the calibration procedure into three parts. First, the electrostatic characteristics of the device are calibrated. The low field mobility is then

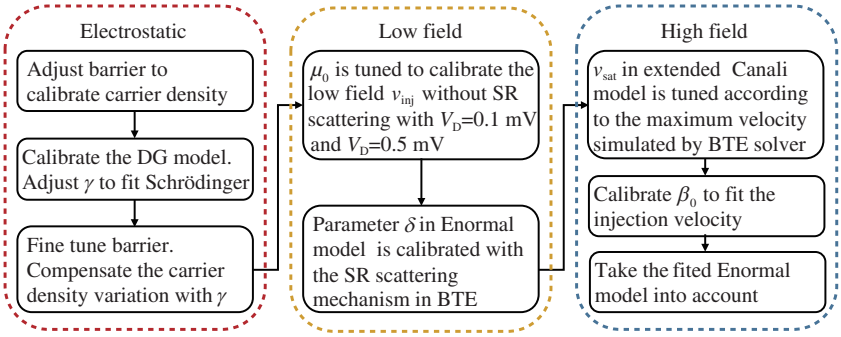

Figure 2 (Color online) Flow chart of the calibration procedure. The procedure consists of three parts, electrostatic characteristics, low field mobility, and high field saturation.

extracted to take into account the effects brought about by the ballistic transport. The last procedure is to calibrate the high field saturation characteristics and consider the velocity overshoot phenomenon. The details of the calibration procedure are shown in Figure 2.

3.1 Calibration of electrostatic characteristics

The electrostatic characteristics of the device are solved using a Poisson-Schrödinger iteration in the BTE solver. The carriers distributed in the device are not only determined by the gate voltage but are also affected by quantum mechanics, which is consistent with the solution of the Schrödinger equation. The carriers distribution in the TCAD simulations, however, is modeled using the density-gradient (DG) model. Consequently, we need to calibrate the DG model using the solution of the Schrödinger equation. An anisotropic DG model is employed to eliminate the quantum effect paralleled with the channel. The effective quantum potential in the DG model is calculated using the equation in [19].

$$\Lambda_n = -\frac{\gamma\hbar^2}{12m_n}\left(\nabla^2 \ln n + \frac{1}{2}\left(\nabla \ln n\right)^2\right), \tag{1}$$

where m_n is the effective mass of the electrons, and n is the carrier density in the device. The magnitude of the quantum effect (the shape of the carrier distribution along the transverse direction) is determined based on the γ parameter. The larger γ is, the more concentrated the carriers are at the middle of the channel. However, the total concentration of the carriers decreases as γ increases, which is different with the solution by the Schrödinger equation. Consequently, we adjust the "barrier" parameter in TCAD to compensate the difference in carrier density between the DG model and the solution by the Schrödinger equation.

During the calibration process, the drain voltage (VD) is set to 0 V, and the carrier distribution in the middle of the channel is calibrated. The relative error vs. γ with different gate voltages is shown in Figure 3. The relative error is derived as

$$\mathrm{err}_{\mathrm{rel}} = \frac{1}{N}\sum_{i=1}^{N}\frac{\left|n^i_{\mathrm{DG}} - n^i_{\mathrm{Sch}}\right|}{n^i_{\mathrm{Sch}}}, \tag{2}$$

where n^i_{DG} and n^i_{Sch} are the carrier density at the ith grid calculated using the DG model and Schrödinger equation, respectively. N is the grid number in the transverse direction.

There exist different optimal values of γ for various V_G. In this case, we choose 0.75 as the value of γ because the accuracy of the model should be guaranteed at higher gate voltages in advance. The relative error of the model with $V_G = 0.4$, 0.5, and 0.6 V are 44.2%, 11.7%, and 19.1%, respectively. The calibration results of the DG model are shown in Figure 4. Good agreements are shown in cases with $V_G = 0.5$ and 0.6 V. Figure 5 shows the total carrier density at the middle of the channel under various gate voltages. Good agreement is shown between the DG model and the solution of the Schrödinger equation. The deviations are caused by the difference between the band structures of the two models

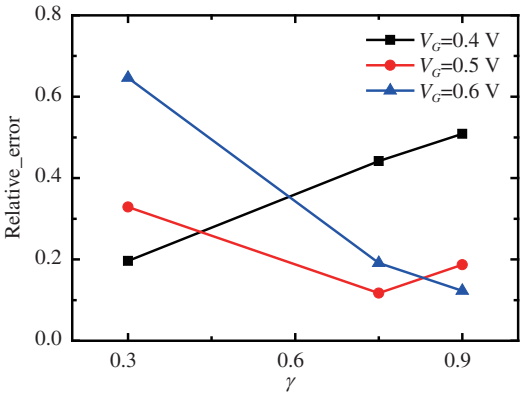

Figure 3 (Color online) Relative error of the calibrated DG model vs. γ parameter under various gate voltages. The drain voltage is set to be zero. The relative error is calculated using the carrier density at the middle of the channel.

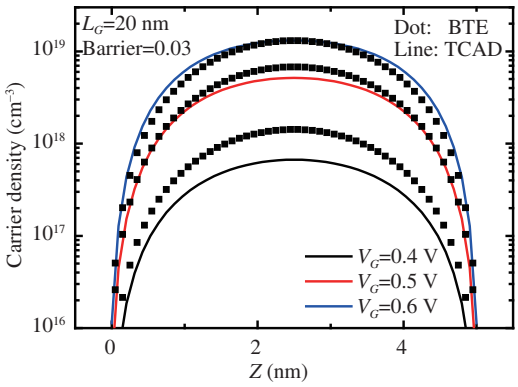

Figure 4 (Color online) Calibration results of the DG model with different gate voltages and V_D=0. The parameter barrier is set to 0.03 to compensate the carrier density variation caused by the DG model.

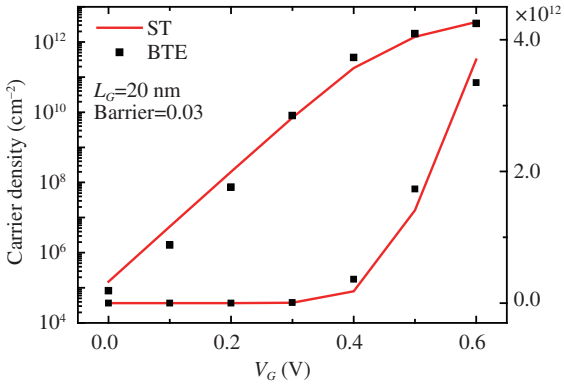

Figure 5 (Color online) Calibration results of the electrostatic characteristics. The relationship between the carrier density in the middle of the channel and the gate voltage is shown in logarithm and linear coordinates, respectively.

employed. In the TCAD tools, a simple band structure is preferred because a complex band structure can lead to an increase in the time consumption. Consequently, we only considered one effective energy valley in the TCAD tool in order to obtain the simulation results in an efficient manner.

3.2 Low field mobility extraction

The second step of the calibration process is to calibrate the low field mobility of the DD model using the results of the BTE solver. As the channel length of the device is only 20 nm, we set the drain voltage to 0.1 and 0.5 mV, respectively, to guarantee that the electric field is sufficiently low. The low field mobility of the transistors worked near the ballistic regime is determined through the long channel low field mobility $\mu_{\rm long}$ and the ballistic mobility $\mu_{\rm bal}$, which were combined using Matthiessen's rule [20]:

$$\frac{1}{\mu_{\rm low}} = \frac{1}{\mu_{\rm long}} + \frac{1}{\mu_{\rm bal}}. \tag{3}$$

In devices with channel lengths of only dozens of nanometers, carriers transport through the channel almost in a ballistic fashion. Consequently, the ballistic mobility, restricted by the injection velocity at the virtual source [21,22], dominates the device. We chose a simple constant mobility model to calibrate the low field mobility of the device. Only phonon scattering mechanisms are involved in this step. The mobility is tuned to calibrate the injection velocity without the effect of the surface roughness scattering (SR). The calibrated velocity along the channel with a gate voltage of 0.6 V is shown in the inset of

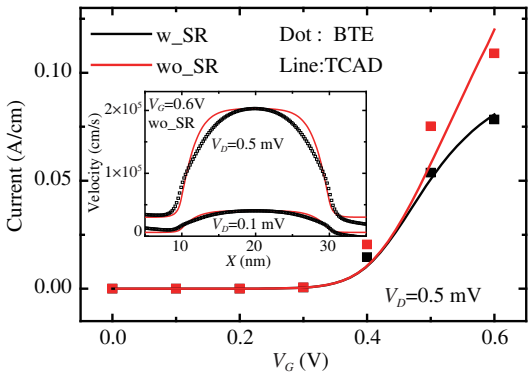

Figure 6 (Color online) Transfer characteristic curve of the device simulated using calibrated low field mobility model and Enormal model. The inset shows the velocity calibration under a small V_D.

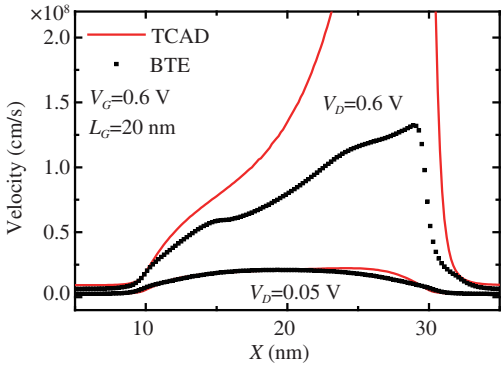

Figure 7 (Color online) Velocity distribution simulated using TCAD and the BTE solver with $V_D = 0.05$ and 0.6 V. A high field saturation model is not involved in the TCAD simulation.

Figure 6. The relative errors of the injection velocity are 0.69% and 0.012% with $V_D = 0.1$ and 0.5 mV, respectively. SR scattering is not involved and good agreement between the calibrated model and the BTE results is obtained. The relative errors of the current at $V_G = 0.4$, 0.5, and 0.6 V are 51.2%, 18.9%, and 10.1%, respectively.

The Enormal model is calibrated using the SR scattering mechanism in the BTE solver once the constant low field mobility is calibrated. The mobility contribution of the surface roughness scattering in the Enormal model is expressed as follows:

$$\mu_{\rm sr} = \left(\frac{F_\perp^2}{\delta} + \frac{F_\perp^3}{\eta}\right), \tag{4}$$

where F is the effective driving force along the transverse direction, and δ and η are the parameters. In this study, the parameter δ is tuned to calibrate the on-current. Figure 6 shows the I_D-V_G curves of the sample with and without considering the effect of SR scattering. When all scattering mechanisms are involved, the relative errors of the calibrated results with $V_G = 0.4$, 0.5, and 0.6 V are 39%, 6.9%, and 3.1%, respectively.

3.3 High field saturation calibration

The calibrated low field mobility is only valid under a small drain voltage. Figure 7 shows the velocity along the channel simulated using TCAD and the BTE solver with a higher V_D. Only the calibrated constant mobility model is involved in the TCAD simulation. The velocity distribution with $V_D = 0.05$ V shows a good agreement. However, the disparity becomes extremely large when V_D is increased to 0.6 V. The maximum velocity along the channel simulated by TCAD is even higher than 8×10^8 cm/s. Consequently, the current with a higher drain voltage in TCAD is also overestimated without considering the high field saturation model.

The conventional high field saturation model is only valid for long channel devices with a saturation velocity of no higher than 1×10^7 cm/s. However, as the gate length scales down to dozens of nanometers, which is comparable to the mean free path of carriers, the velocity overshoot phenomenon must be considered by the model. If a conventional high field saturation model is employed in a modern device simulation, the velocity may be saturated at 1×10^7 cm/s from the beginning of the channel. As a result, the drive current simulated by the conventional model is far smaller than the real current. Consequently, it is indispensable to calibrate the parameters in a high field saturation model.

There are two high field saturation models of choice, namely, the extended Canali model [23] and the

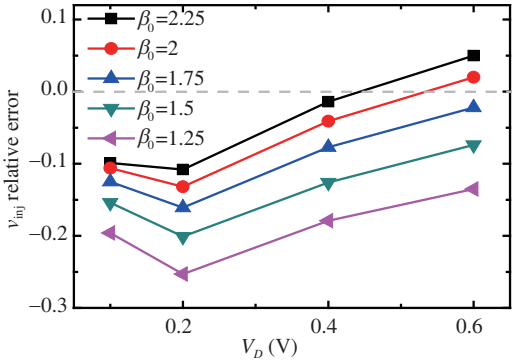

Figure 8 (Color online) The relative error of the injection velocity with various parameters β_0.

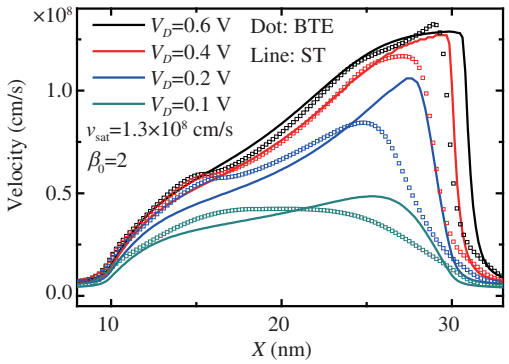

Figure 9 (Color online) Calibration of velocity along the channel under $V_G = 0.6$ V. The injection velocity is the key point.

transferred electron model [24]. The formula of the extended Canali model is

$$\mu(F) = \frac{\mu_{\text{low}}}{\left[1 + \left(\frac{\mu_{\text{low}} F}{v_{\text{sat}}}\right)^{\beta}\right]^{1/\beta}}, \tag{5}$$

where β is a parameter related to the thermal characteristics, and is expressed as

$$\beta = \beta_0 \left(\frac{T}{300K}\right)^{\beta_{\text{exp}}}, \tag{6}$$

where T is the temperature of the device. In addition, β_0 and β_{exp} are the parameters, v_{sat} is the saturation velocity, F is the electric field along the channel, and the parameter μ_{low} is the calibrated low field mobility during the previous step.

The transferred electron model considers the effect of inter-valley scattering in the III-V materials, which is derived as

$$\mu = \frac{\mu_{\text{low}} + \left(\frac{v_{\text{sat}}}{F}\right)\left(\frac{F}{E_0}\right)^4}{1 + \left(\frac{F}{E_0}\right)^4}. \tag{7}$$

The velocity reaches the maximum value when the longitudinal electric field is near E_0, and then gradually decreases with the electric field, finally saturating at the saturation velocity v_{sat}.

After a careful comparison, we chose the extended Canali model because with the transferred electron model, the separation between the maximum velocity and v_{sat} is difficult to adjust by tuning the parameters, and moreover, the declination of the saturation velocity associated with inter-valley scattering is trivial in InGaAs, whose band gap between the Γ valley and L valleys is as large as 0.67 eV. Such a large band gap guarantees that few carriers are scattered to L valleys during the transport process.

The parameter v_{sat} and β_0 are tuned to calibrate the velocity along the transport direction. According to the top-of-the-barrier (ToB) theory, the injection velocity is the key point to be calibrated. The v_{sat} parameter is set according to the maximum velocity simulated using the BTE solver to describe the velocity overshoot phenomenon. For this sample, the the v_{sat} parameter is 1.3×10^8 cm/s. Figure 8 shows the relative error of v_{inj} under various V_D with different values of β_0. It can be observed that the injection velocity is higher with a larger β_0, and the model is more accurate under a higher V_D. As a result, the value of β_0 is set to 2 because a smaller relative error is shown in saturate state. Figure 9 shows the calibration results of the velocity distribution along the channel under various values of V_D. Compared with the conventional model, the calibrated model has a much better agreement with the results of the BTE solver, particularly under a higher V_D. For the lower V_D cases, the deviation in the maximum velocity is relatively larger. The calibration of the output characteristic curves with the

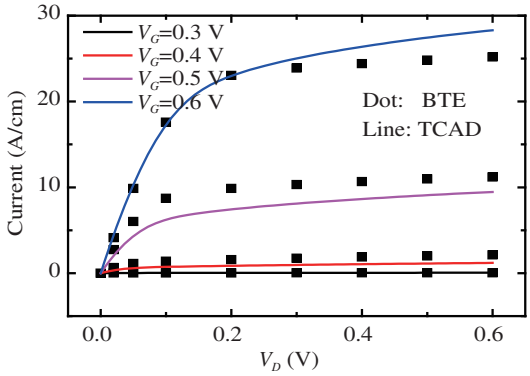

Figure 10 (Color online) Calibration results of output characteristics curves with calibrated high field saturation model.

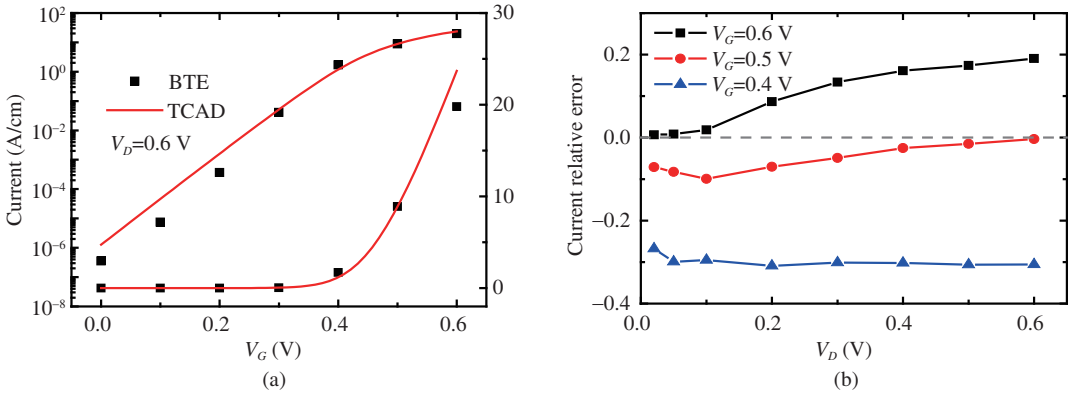

Figure 11 (Color online) (a) Transfer characteristic curve in logarithm and linear coordinates and (b) relative error of the current under various biases after the Enormal model is involved.

Table 2 Relative error of every step of the calibration procedure

Procedure	Relative error		
	$V_G = 0.4$ V	$V_G = 0.5$ V	$V_G = 0.6$ V
DG model	44.2%	11.7%	19.1 %
Low field $v_{\rm inj}$		0.69% and 0.012% with $V_D = 0.1$ and 0.5 mV	
Low field current	51.2%	18.9%	10.1 %
Low field Enormal	39%	6.9%	3.1 %
High field $v_{\rm inj}$		2.7% with $V_D = 0.6$ V	
High field current	43.7%	12.5%	12.3 %
High field Enormal	29.4%	1.2%	19.7 %

calibrated high field saturation model is shown in Figure 10. The relative error of the current under $V_D = 0.6$ V is -12.5% with $V_G = 0.5$ V, and 12.3% with $V_G = 0.6$ V.

Finally, we take the Enormal model into account, the parameters of which were previously calibrated in the previous step. The calibration of the transfer characteristic curve is shown in Figure 11(a), and Figure 11(b) shows the relative error of the current calibration under different biases. At $V_G = 0.6$ V, the relative error is almost zero in the linear region but gradually increases to 19.7% with an increase in the drain voltage. For other cases, this trend is relatively flat. We have extracted the relative errors of the calibration for every step shwon in Table 2. The relative error of every step is approximately consistent with that of the carrier density, which is caused by the difference between band structures employed by the BTE solver and the TCAD tools.

4 Conclusion

We proposed a systematic calibration procedure of the DD model for InGaAs MOSFETs operating in the ballistic regime. The electrostatic characteristics, low field mobility, and high field saturation model were calibrated following a particular sequence. The agreement between the calibrated DD model and the BTE solver is acceptable, and the deviation of the drive current is approximately consistent with that of the carrier density calibrated in the first step, which is caused by the difference in band structures employed by the BTE solver and the TCAD tools.

Acknowledgements This work was supported by National Natural Science Foundation of China (Grant Nos. 61674008, 61421005, 61404005).

References

1 Deleonibus S. Looking into the future of Nanoelectronics in the Diversification Efficient Era. Sci China Inf Sci, 2016, 59: 061401
2 Cheng K, Khakifirooz A. Fully depleted SOI (FDSOI) technology. Sci China Inf Sci, 2016, 59: 061402
3 Natori K, Iwai H, Kakushima K. Anomalous degradation of low-field mobility in short-channel metal-oxide-semiconductor field-effect transistors. J Appl Phys, 2015, 118: 234502
4 Khandelwal S, Agarwal H, Kushwaha P, et al. Unified compact model covering drift-diffusion to ballistic carrier transport. IEEE Electron Device Lett, 2016, 37: 134–137
5 Jin S, Pham A-T, Choi W, et al. Performance evaluation of FinFETs: from multisubband BTE to DD calibration. In: Proceedings of International Conference Simulation Semicond Processes Devices, 2016. 109–116
6 Iwai H, Natori K, Shiraishi K, et al. Si nanowire FET and its modeling. Sci China Inf Sci, 2011, 54: 1004–1011
7 Xie Q, Xu J. Recent research development of FinFETs. Sci China-Phys Mech Astron, 2016, 59: 127331
8 Takagi S, Takenaka M. Ge/III-V MOS device technologies for low power integrated systems. In: Proceedings of Solid State Device Research Conference (ESSDERC), 2015. 20–25
9 Vardi A, Zhao X, del Alamo J A. Quantum-size effects in sub 10-nm fin width InGaAs FinFETs. In: Proceedings of IEEE International Electron Devices Meeting, 2015. 1–4
10 Kim D-H, Kim T-W, Back R H, et al. High-performance III-V devices for future logic applications. In: Proceedings of IEEE International Electron Devices Meeting, 2014. 1–4
11 del Alamo J A. Nanometre-scale electronics with III-V compound semiconductors. Nature, 2011, 479: 317–323
12 Beneventi G B, Reggiani S, Gnudi A, et al. A TCAD low-field electron mobility model for thin-body InGaAs on InP MOSFETs calibrated on experimental characteristics. IEEE Trans Electron Devices, 2015, 62: 3645–3652
13 Lu T, Du G, Liu X, et al. A finite volume method for the multi subband boltzmann equation with realistic 2D scattering in double gate MOSFETs. Commun Commut Phys, 2011, 10: 305–338
14 Di S, Zhao K, Lu T, et al. Investigation of transient responses of nanoscale transistors by deterministic solution of the time-dependent BTE. J Comput Electron, 2016, 15: 770–777
15 Di S, Shen L, Chang P, et al. Performance comparison of Si, III-V double-gate n-type MOSFETs by deterministic Boltzmann transport equation solver. Jpn J Appl Phys, 2017, 56: 04CD08
16 Smirnov S. Physical modeling of electron transport in strained silicon and silicon-germanium. Dissertation for Ph.D. Degree. Wien: Fakultät für Elektrotechnik und Informationstechnik, 2003
17 Esseni D. On the modeling of surface roughness limited mobility in SOI MOSFETs and its correlation to the transistor effective field. IEEE Trans Electron Dev, 2004, 51: 394–401
18 Fischetti M V. Monte Carlo simulation of transport in technologically significant semiconductors of the diamond and zinc-blende structures. I - Homogeneous transport. IEEE Trans Electron Devices, 1991, 38: 634–649
19 Ancona M G, Iafrate G J. Quantum correction to the equation of state of an electron gas in a semiconductor. Phys Rev B, 1989, 39: 9536–9540
20 Shur M S. Low ballistic mobility in submicron HEMTs. IEEE Electron Device Lett, 2002, 23: 511–513
21 Lundstrom M. Elementary scattering theory of the Si MOSFET. IEEE Electron Device Lett, 1997, 18: 361–363
22 Rahman A, Lundstrom M S. A compact scattering model for the nanoscale double-gate MOSFET. IEEE Trans Electron Dev, 2002, 49: 481–489
23 Canali C, Majni G, Minder R, et al. Electron and hole drift velocity measurements in silicon and their empirical relation to electric field and temperature. IEEE Trans Electron Dev, 1975, 22: 1045–1047
24 Barnes J J, Lomax R J, Haddad G I. Finite-element simulation of GaAs MESFET's with lateral doping profiles and submicron gates. IEEE Trans Electron Dev, 1976, 23: 1042–1048